

Journal of Biomedical Optics

SPIEDigitalLibrary.org/jbo

Ultrastructural alterations in field carcinogenesis measured by enhanced backscattering spectroscopy

Andrew J. Radosevich
Nikhil N. Mutyal
Ji Yi
Yolanda Stypula-Cyrus
Jeremy D. Rogers
Michael J. Goldberg
Laura K. Bianchi
Shailesh Bajaj
Hemant K. Roy
Vadim Backman

Ultrastructural alterations in field carcinogenesis measured by enhanced backscattering spectroscopy

Andrew J. Radosevich,^a Nikhil N. Mutyal,^a Ji Yi,^a Yolanda Stypula-Cyrus,^a Jeremy D. Rogers,^a Michael J. Goldberg,^c Laura K. Bianchi,^c Shailesh Bajaj,^c Hemant K. Roy,^b and Vadim Backman^a

^aNorthwestern University, Department of Biomedical Engineering, Tech E310, 2145 Sheridan Road, Evanston, Illinois 60208

^bBoston Medical Center, Department of Medicine, Boston, Massachusetts 02118

^cNorthShore University HealthSystems, Department of Internal Medicine, Evanston, Illinois 60201

Abstract. Optical characterization of biological tissue in field carcinogenesis offers a method with which to study the mechanisms behind early cancer development and the potential to perform clinical diagnosis. Previously, low-coherence enhanced backscattering spectroscopy (LEBS) has demonstrated the ability to discriminate between normal and diseased organs based on measurements of histologically normal-appearing tissue in the field of colorectal (CRC) and pancreatic (PC) cancers. Here, we implement the more comprehensive enhanced backscattering (EBS) spectroscopy to better understand the structural and optical changes which lead to the previous findings. EBS provides high-resolution measurement of the spatial reflectance profile $P(r_s)$ between 30 microns and 2.7 mm, where information about nanoscale mass density fluctuations in the mucosa can be quantified. A demonstration of the length-scales at which $P(r_s)$ is optimally altered in CRC and PC field carcinogenesis is given and subsequently these changes are related to the tissue's structural composition. Three main conclusions are made. First, the most significant changes in $P(r_s)$ occur at short length-scales corresponding to the superficial mucosal layer. Second, these changes are predominantly attributable to a reduction in the presence of subdiffractional structures. Third, similar trends are seen for both cancer types, suggesting a common progression of structural alterations in each. © The Authors.

Published by SPIE under a Creative Commons Attribution 3.0 Unported License. Distribution or reproduction of this work in whole or in part requires full attribution of the original publication, including its DOI. [DOI: [10.1117/1.JBO.18.9.097002](https://doi.org/10.1117/1.JBO.18.9.097002)]

Keywords: enhanced backscattering; coherent backscattering; inverse scattering; optical properties; elastic light scattering; spectroscopy; colorectal cancer; pancreatic cancer.

Paper 130408R received Jun. 12, 2013; revised manuscript received Jul. 16, 2013; accepted for publication Aug. 7, 2013; published online Sep. 5, 2013.

1 Introduction

Cancer is a multistep process in which a number of smaller mutations accumulate in a stepwise fashion that eventually leads to carcinoma and metastasis. One way to conceptualize this process is through the notion of field carcinogenesis.¹ Under this approach to understanding carcinogenesis, several genetic/epigenetic mutations are expressed diffusely throughout a diseased organ as subtle ultrastructural transformations that constitute a “fertile field” from which further cancer progression can arise. From within this field, localized neoplasia with malignant potential emerge through stochastic mutations.

Although the concept of field carcinogenesis has been under study since 1953, the ultrastructural changes that compose the field are still being uncovered. Several changes whose role in field carcinogenesis has been implicated include chromatin condensation,^{2–4} cytoskeleton disruption,⁵ and collagen cross-linking in the extracellular matrix.⁶ Still, the exact origin and carcinogenic advantage these transformations confer are not fully understood.

The implications of more fully understanding the mechanisms behind field carcinogenesis are twofold. First, it provides a glimpse into cancer development at the earliest stages. Such information can form a basis from which the later stages of

cancer can be better understood, and offers the potential for identifying common origins behind all cancer types. Second, it can be exploited to accurately detect the presence of cancer at less invasive surrogate sites away from the location of neoplasia. Moreover, detection of this kind could be performed at an early stage where more treatment options are available and prognosis is vastly improved.

One technique that enables exploration into both implications is optical characterization of biological tissue using enhanced backscattering (EBS) spectroscopy, also known as coherent backscattering.⁷ EBS is observed as an angular backscattering peak whose shape is the two-dimensional (2-D) Fourier transform of the spatial reflectance profile $P(\vec{r}_s)$, where \vec{r}_s represents a relative spatial separation between the entrance and exit point of any multiply scattered ray in the medium. Previously, a variation on EBS known as low-coherence enhanced backscattering (LEBS) spectroscopy has demonstrated an ability to sense the structural alterations occurring in field carcinogenesis.⁸ LEBS uses partial coherence illumination to selectively interrogate $P(r_s)$ at subdiffusion length-scales ($r_s < 1$ transport mean free path). In a study of histologically normal rectal biopsies from 219 subjects undergoing colorectal cancer (CRC) screening, LEBS detected the presence of adenomatous polyps >10 mm in diameter throughout the colon with 100% sensitivity, 80% specificity, and 89.5% area under the receiver operator characteristic curve (AUROC).⁹ In another study of histologically normal duodenal biopsies from 203 subjects undergoing upper endoscopy, LEBS detected the presence of pancreatic carcinomas with 95% sensitivity,

Address all correspondence to: Andrew J. Radosevich, Northwestern University, Department of Biomedical Engineering, Tech E310, 2145 Sheridan Road, Evanston, IL 60208. Tel: +847-467-3215; Fax: (847) 491-4928; E-mail: arad@u.northwestern.edu

71% specificity, and 85% AUROC.¹⁰ These studies demonstrated the proof of principle that LEBS could detect the changes occurring in human CRC and pancreatic cancer (PC) field carcinogenesis. However, the LEBS instrumentation used in these studies was limited in two respects. First, it was not capable of identifying the structural and optical origin of the measured changes. Second, it could not be implemented for *in vivo* application.

To address these needs, two incarnations of the EBS instrumentation are currently being developed. First, a bench-top instrument provides comprehensive measurement of the shape of $P(r_s)$ within both the subdiffusion and diffusion regimes with high spatial resolution ($\sim 4 \mu\text{m}$).^{7,11} Measurements of this kind are extremely sensitive to the shape of the scattering phase function,¹² which contains information about the subtle structural alterations occurring in field carcinogenesis at structural length-scales down to $\sim 30 \text{ nm}$ (Ref. 13). Second, a 3.4 mm diameter probe-based LEBS instrument trades comprehensive measurement of $P(r_s)$ for the ability to fit inside the working channel of commercially available endoscopes.¹⁴ This configuration targets aspects of $P(r_s)$ that have demonstrated diagnostic potential and has been presented for use in CRC and PC risk stratification.^{15–17}

In this paper, we implement the comprehensive bench-top EBS instrument to study the structural origin behind the changes previously observed in CRC and PC field carcinogenesis. The paper is organized as follows: In Sec. 2, we review the fundamentals of scattering theory in random media under the Born approximation and the theoretical origin of the EBS phenomenon. Next, in Sec. 3, we detail the EBS instrument and data processing, the use of EBS to extract ultrastructural and optical properties from experimental measurements, the experimental procedure used in our biopsy study, and the steps needed to generate a 2-D random medium. In Sec. 4, we implement EBS to determine the length-scales at which $P(r_s)$ is optimally altered, quantify the structural and optical alterations that lead to such changes, and estimate which depths contribute to the observed alterations. Finally, the conclusions are summarized in Sec. 5.

2 Theory

2.1 Scattering Theory: Born Approximation in Continuous Random Media

In this section, we briefly review the application of the Born approximation in a continuous random media to calculate

the scattering characteristics needed for the current study. Comprehensive discussion of scattering theory under the Born approximation can be found in Chapter 13 of Ref. 18, Chapter 7 of Ref. 19, and Chapter 6 of Ref. 20. A more specific treatment for continuous random media is found in Chapter 16 of Ref. 21. Application to biological tissue using the Whittle-Matérn family of autocorrelation functions was first presented in Refs. 22 and 23.

Scattering contrast within biological tissue is generated by the random arrangement of a number of arbitrarily shaped structures ranging in size from tens of nanometers to tens of microns.²⁴ The best way to mathematically describe such a randomly distributed media is through its statistical refractive index autocorrelation function $B_n(r_d)$. One versatile model to describe $B_n(r_d)$ uses the three-parameter Whittle-Matérn family of autocorrelation functions.^{22–25}

$$B_n(r_d) = A_n \cdot \left(\frac{r_d}{L_n}\right)^{\frac{D-3}{2}} \cdot K_{\frac{D-3}{2}}\left(\frac{r_d}{L_n}\right), \quad (1)$$

where the subscript on r_d implies a differential separation between any two points, A_n is the amplitude of refractive index fluctuations [i.e., scales $B_n(r_d)$ along y axis], L_n is the characteristic distribution length [i.e., scales $B_n(r_d)$ along x axis], and D determines the shape of the distribution. For $r_d < L_n$, $B_n(r_d)$ approaches a power law when $0 < D < 3$, a decaying exponential when $D = 4$, and a Gaussian as $D \rightarrow \infty$. Depictions of the spatial distribution of refractive index specified by $B_n(r_d)$ for three values of D are shown in Fig. 1.

In this paper, we refer to A_n , L_n , and D as ultrastructural properties since they govern the spatial distribution of sub-diffractive fluctuations in refractive index. Additionally, we refer to values of r_d as structural length-scales (e.g., sub-diffractive information is carried at short structural length-scales below $\sim \lambda/2$).

In order to relate $B_n(r_d)$ to light scattering, we apply the first Born approximation to calculate the power spectral density Φ_s as the three-dimensional (3-D) Fourier transform of $B_n(r_d)$.²¹ For the Whittle-Matérn model, Φ_s can be calculated analytically as²²

$$\Phi_s(k_s) = \frac{A_n L_n^3 \Gamma(\frac{D}{2})}{\pi^{3/2} 2^{(5-D)/2}} \cdot (1 + k_s^2 L_n^2)^{-D/2}, \quad (2)$$

where $k_s = 2k \sin \frac{\theta}{2}$ and k is the wavenumber.

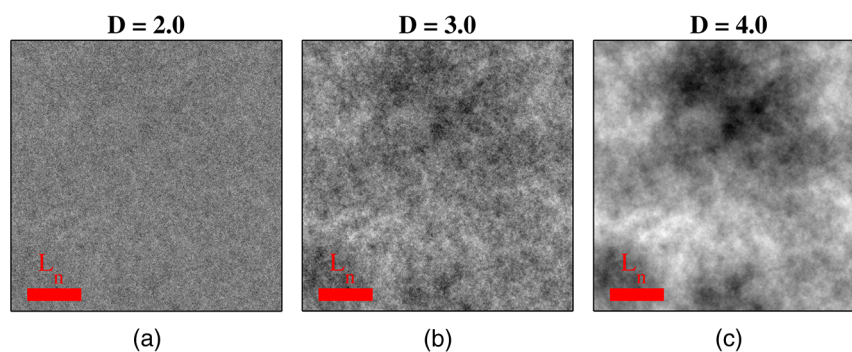


Fig. 1 Demonstration of the random media specified by the Whittle-Matérn model for (a) $D = 2$, (b) $D = 3$, and (c) $D = 4$. The methods used to generate these images are described in Sec. 3.3.

In order to describe the directionality of scattered light intensity, the differential scattering cross-section per unit volume for unpolarized light $\sigma(\theta)$ can be calculated by multiplying $\Phi_s(k_s)$ by the dipole radiation pattern.

$$\sigma(\theta) = 2\pi k^4 (1 + \cos^2 \theta) \Phi_s(2k \sin \frac{\theta}{2}). \quad (3)$$

The shape of $\sigma(\theta)$ can be parametrized by the scattering mean free path l_s (i.e., inverse of the scattering coefficient μ_s) and the anisotropy factor g (i.e., how forward directed the scattering is).²⁰

$$l_s = \left[2\pi \int_{-1}^1 \sigma(\cos \theta) d \cos \theta \right]^{-1}, \quad (4)$$

$$g = 2\pi l_s \int_{-1}^1 \cos \theta \cdot \sigma(\cos \theta) d \cos \theta. \quad (5)$$

Finally, the effective transport for a diffusely scattering medium is expressed by the transport mean free path.

$$l_s^* = \frac{l_s}{1 - g}. \quad (6)$$

We refer to l_s , g , and l_s^* as optical properties.

Analytical equations relating the ultrastructural and optical properties under the Whittle-Matérn model can be found in Ref. 22. One relationship that is useful to describe in further detail is that between l_s^* and D . In the limit of $kL_n \gg 1$,

$$l_s^*(k) \propto k^{D-4} \quad \text{for } D < 4. \quad (7)$$

In words, this means that for $D < 4$, the spectral dependence of l_s^* follows a power-law distribution whose power is solely dependent on D . In this way, although D should primarily be thought of as an ultrastructural property, it is also conceptually useful to think of it as an optical property that determines how strongly light transport changes with illumination wavelength.

2.2 Enhanced Backscattering Theory

In this section, we briefly review the theoretical aspects of EBS that are pertinent to the discussion in the following sections. Additional details concerning the origin of EBS can be found

in a number of seminal publications on the first experimental observation of EBS.²⁶⁻²⁹ More recently, publications from our group detail the application of EBS to biological tissue characterization. These publications include an open source Monte Carlo program,³⁰ detailed description of the bench-top instrument used to measure biological tissue,⁷ description of the measurement of the spatial reflectance profile using EBS,¹¹ description of an inverse method to extract optical properties,³¹ and development of a miniaturized probe-based LEBS instrument to characterize tissue *in vivo*.¹⁴

The EBS signal is an angular intensity peak [$I_{\text{EBS}}(\theta_x, \theta_y)$, see Fig. 2(a)] with its maximum value centered in the backscattering direction. The origin of $I_{\text{EBS}}(\theta_x, \theta_y)$ is the constructive interference between all time-reversed path-pairs within a scattering medium. Mathematically, the interference signal from all path-pairs exiting the medium within the illumination spot can be summed using a Fourier transform operation to obtain the total observable signal.⁷

$$\begin{aligned} I_{\text{EBS}}(\theta_x, \theta_y) &= \iint_{-\infty}^{\infty} P(x_s, y_s) \\ &\cdot S(x_s, y_s) e^{ik(x_s \sin \theta_x + y_s \sin \theta_y)} dx_s dy_s, \\ &= \mathcal{F}\{P(x_s, y_s) \cdot S(x_s, y_s)\}, \end{aligned} \quad (8)$$

where the subscript on x_s and y_s implies a relative separation between any two points, $P(x_s, y_s)$ is the spatial distribution of all multiply scattered photons (i.e., two or more scattering events) exiting the medium in the exact backscattering direction (i.e., antiparallel to the incident beam), $S(x_s, y_s)$ modulates the shape due to finite spot-size illumination, and \mathcal{F} represents the Fourier transform operation.

Of primary interest for tissue characterization is function $P(x_s, y_s)$, commonly known by a number of different names including spatially resolved diffuse reflectance,^{32,33} spatial backscattering impulse-response,¹¹ diffuse reflectance profile, etc. While there are a great many instruments that measure some aspect of $P(x_s, y_s)$,³⁴⁻³⁶ part of the power of using EBS is that it provides noncontact measurement of $P(x_s, y_s)$ at very short length scales ranging from $(y_s, x_s) = \pm 30 \mu\text{m}$ to $\pm 2.7 \text{ mm}$ with $\sim 4 \mu\text{m}$ spatial resolution.¹¹ This range of length scales enables comprehensive characterization of $P(x_s, y_s)$ within both the subdiffusion ($\sqrt{x_s^2 + y_s^2} < l_s^*$) and diffusion regimes, allowing for accurate extraction of all three ultrastructural and optical properties.

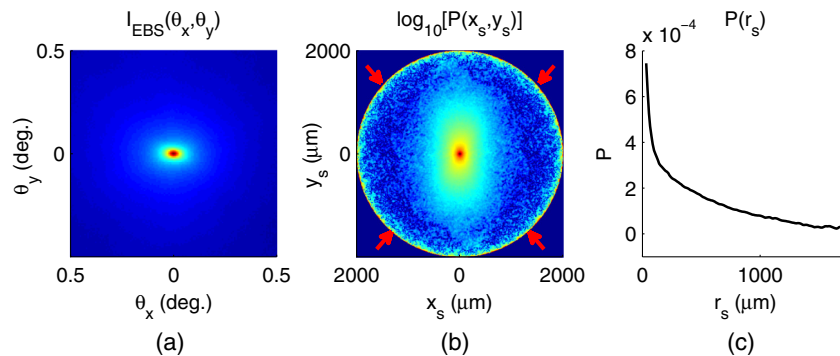


Fig. 2 Example data showing average measurements from all colorectal cancer (CRC) control biopsy samples. (a) measured at $\lambda = 700 \text{ nm}$. (b) Log-scale $P(x_s, y_s)$ obtained through inverse Fourier transform. The red arrows indicate inaccuracies in the measurement of $P(x_s, y_s)$ due to noise amplification as described in Sec. 3.1. (c) distribution obtained after integration over the azimuthal angle.

3 Materials and Methods

3.1 EBS Instrument and Data Processing

Detailed description and schematics for our EBS instrument can be found in Refs. 7 and 13. In brief, broadband visible light from a supercontinuum laser source (SuperK Extreme EXW-6, NKT Photonics A/S, Birkerød, Denmark) is coupled into a single-mode fiber (Thorlabs, Newton, New Jersey; mode field diameter of 4.6 μm at 680 nm) and collimated to an ~ 10 mm beam diameter. The beam then passes through a linear polarizer and an iris that reduces its diameter to 2 mm in size before being directed onto the biopsy. Light backscattered from the sample is then collected by a 50/50 nonpolarizing antireflection coated plate beam splitter, passes through a linear polarizer to detect the copolarized channel, and is focused onto a CCD camera (PIXIS 1024B eXcelon, Princeton Instruments, Trenton, New Jersey) by a 100 mm focal length achromatic lens. A liquid crystal tunable filter (VariSpec, PerkinElmer, Waltham, Massachusetts) attached to the camera separates the light into its component wavelengths. This configuration detects angular backscattering of up to 7.5776 deg with 0.0074 deg resolution and wavelengths between 500 and 720 nm with a 20 nm filter bandwidth. After inverse Fourier transform, this provides a minimum spatial resolution of 3.78 μm (at $\lambda = 500$ nm) and a maximum spatial range of 5.42 mm (at $\lambda = 700$ nm).

To process the data, the biopsy measurement is first background subtracted and then normalized by the total unpolarized incoherent intensity measured from a reflectance standard (spectralon >98% reflectance, Ocean Optics, Dunedin, Florida). $I_{\text{EBS}}(\theta_x, \theta_y)$ is then obtained by subtracting the incoherent baseline with a plane fit, using data from an annular ring that is ~ 1.8 deg away from the peak maximum. An example of the peak shape measured from a rectal biopsy with illumination in the linear copolarized configuration is shown in Fig. 2(a).

The angular data are then converted to spatial coordinates through inversion of Eq. (8) to obtain^{7,13,37}

$$P(x_s, y_s) = \frac{\mathcal{F}^{-1}I_{\{\text{EBS}\}}(\theta_x, \theta_y)}{S(x_s, y_s)}, \quad (9)$$

where function S can be computed as the autocorrelation of the spatial illumination distribution incident on the biopsy normalized to unity at the origin. Assuming the beam intensity is a top-hat function with diameter \emptyset , function S is found analytically as⁷

$$S(x_s, y_s) = \begin{cases} \frac{2\emptyset^2 \cos^{-1}(\sqrt{x_s^2 + y_s^2}/\emptyset) - 2\sqrt{(x_s^2 + y_s^2)(\emptyset^2 - x_s^2 - y_s^2)}}{\emptyset^2 \pi} & \text{for } \sqrt{x_s^2 + y_s^2} < \emptyset \\ 0 & \text{for } \sqrt{x_s^2 + y_s^2} > \emptyset \end{cases} \quad (10)$$

Figure 2(b) shows the $P(x_s, y_s)$ distribution extracted from the measurement of $I_{\text{EBS}}(\theta_x, \theta_y)$ in Fig. 2(a).

As a way to average noise and make it easier to display experimental results, we integrate $P(x_s, y_s)$ over the azimuthal angle to obtain $P(r_s)$.

$$P(r_s) = \int_0^{2\pi} P(x_s = r_s \cos \phi, y_s = r_s \sin \phi) d\phi. \quad (11)$$

In words, $P(r_s)$ represents the total reflected intensity that exits the medium in the backscattering direction within an

annulus of radius r_s . Figure 2(c) shows the $P(r_s)$ distribution calculated from $P(x_s, y_s)$ in Fig. 2(b). Matlab code performing the operations in Eqs. (9) to (11) are posted on our laboratory website.³⁸

We note that since function S decays to 0 for $r_s > \emptyset$, the measurement of $P(r_s)$ is physically limited to length-scales smaller than \emptyset (2 mm in our case). Moreover, division by the decaying function S increasingly amplifies noise at increasing r_s , making the measurement inaccurate as $r_s \rightarrow \emptyset$ [indicated by red arrows in Fig. 2(b)]. As such, in this paper, we only plot the shape of $P(r_s)$ for length-scales in which function S is $> 5\%$. This occurs at $\sim 0.88\emptyset$, or, in our case 1760 μm .

3.2 EBS Extraction of Ultrastructural and Optical Properties

Determination of the ultrastructural and optical properties of each biopsy sample is performed by fitting the shape of $P(r_s)$ to the Whittle-Matérn model. This process was first presented in Ref. 7. Briefly, a series of Monte Carlo simulations using the open source code detailed in Ref. 30 was performed in order to generate a library of $P(r_s)$ for $D = 2.0$ to 4.0 in 0.1 steps, $g = 0.70$ to 0.96 in 0.02 steps, and $r_s/l_s^* = 0.004$ to 4 in 0.004 steps. Through use of multidimensional interpolation, we are able to rapidly generate $P(r_s)$ for arbitrary optical properties within the library bounds. In order to extract the three ultrastructural properties, we minimize the sum squared error between the experimentally measured and library-generated $P(r_s) \cdot S(r_s)$ using a gradient search method in Matlab. We fit each curve over the values of r_s for which we see a significant difference between case and control. To avoid the contribution of absorption, we fit the data using the wavelength range from 600 to 700 nm. Within this range, the contribution from absorption is $\sim 1\%$ that of scattering in the mucosa and is therefore negligible. The three ultrastructural properties can then be converted to optical properties at each wavelength using the analytical equations in Ref. 22.

It is important to make note of two assumptions/limitations inherent in our fitting routine. First, the Monte Carlo simulations are performed for the index matching case, and therefore assume that there is no refractive index contrast at the boundary. In order to account for this in our model, we use an empirically derived scaling factor to adjust the magnitude of the Monte Carlo simulated $P(r_s)$. Second, our model assumes a single slab geometry. As such, this technique is not capable of separating the contribution of layers with varying ultrastructural properties and instead provides measurement of the bulk optical properties within the slab.

3.3 Generation of Random Medium Realizations

To generate a single 2-D realization of the random media specified by $B_n(r_d)$, the following steps can be followed: First, calculate the 2-D Fourier transform of $B_n(r_d)$ and take the square root. This specifies the distribution of spatial frequencies present in the medium. Second, multiply the resulting function by a 2-D Gaussian white noise signal with 0 mean and a variance of 1. This creates randomness within the spatial frequency domain. Finally, return to spatial coordinates by calculating the inverse 2-D Fourier transform and add the real and imaginary components. Microscopic resolution renderings can be made by multiplying the spatial frequency domain function by an area

normalized top-hat function with radius $k \cdot \text{NA}$, where NA is the desired numerical aperture.

3.4 Experimental Biopsy Measurement Procedure

Two to three pinch biopsies (~ 2 to 3 mm diameter) were taken from subjects undergoing normal endoscopic screening procedures in accordance with the institutional review board at NorthShore University HealthSystems. Biopsies < 2 mm in diameter were not measured since they were smaller than the illumination beam diameter. For the CRC study, biopsies were collected from histologically normal sites within the rectal mucosa of subjects undergoing colonoscopy. Progression of field carcinogenesis was categorized according to the size of the largest adenomatous polyp found during colonoscopy and verified by a hospital pathologist. Four groups were assigned: healthy control (C, $N = 43$) with no adenomatous polyps found during colonoscopy, diminutive adenomas (DA, $N = 6$) with diameter < 5 mm, adenomas (A, $N = 25$) with diameter from 5 to 9 mm, and advanced adenomas (AA, $N = 19$) with diameter > 10 mm or adenocarcinoma. For the PC study, biopsies were collected from histologically normal periampullary duodenum of subjects undergoing upper endoscopy procedures. Subjects were categorized into two groups: healthy controls (C, $N = 13$) included individuals without any personal/family history of cancer or pancreato-biliary disease and the PC group ($N = 19$) included subjects harboring adenocarcinomas.

Biopsies from all subjects were transported to Northwestern University in phosphate buffered saline (PBS) solution and measured within 4 h of extraction. A minimum of five spectral EBS measurements ($\lambda = 500$ to 700 nm in 20 nm steps) were acquired from the epithelial side of each biopsy. To prepare the sample for measurement, it was placed in the center of a glass slide, oriented with the epithelium facing upward, and covered with PBS. Two 1-mm spacers were then placed on either side of the biopsy and then covered with a 165- μm glass cover-slip. This served to (1) ensure a uniform 1 mm thickness between all measurements, (2) maintain hydration for the experiment duration, and (3) direct the specular reflection away from the detector.

After measurement with EBS, the biopsies were fixed in 10% formalin for a minimum of 24 h. The samples were then

embedded in paraffin wax and sectioned (5 μm) according to standard protocols. Slides were stained with hematoxylin and eosin and imaged using a 10 \times microscope objective.

4 Results

4.1 $P(r_s)$ in Colorectal Cancer and Pancreatic Cancer

Figure 3 shows the changes in $P(r_s)$ attributable to CRC field carcinogenesis measured in *ex vivo* rectal biopsies. The general shape of $P(r_s)$ in these biopsies is a strongly decaying function of r_s with $\sim 90\%$ of the intensity falling within the first 1000 μm shown in Fig. 3(a). Going from the curve for control subjects (C) to those harboring advanced adenomas (AA), there is a downward and inward shift of $P(r_s)$, indicated by the black arrow. The center and thickness of each curve indicate the mean and standard error, respectively. Performing a two-tailed student's *t*-test at each r_s , we find a statistical significance for values of r_s ranging from ~ 150 to 700 μm [shown as the shaded gray region in Fig. 3(a)].

In order to better visualize the location and magnitude of these changes, Fig. 3(b) shows the difference between $P(r_s)$ for control and AA subjects. For smaller values of r_s , the effect increases in magnitude, consistent with the argument that the alterations associated with field carcinogenesis are most pronounced in the superficial mucosal layers.⁴ As a way to determine the r_s location with the most significant changes, we find the location in which the p-value is minimized. This value ($r_{s,\text{optimal}}$) is found at 267 μm and indicated as the dotted circle in Fig. 3(b).

Finally, to demonstrate the magnitude of the effect during the early progression of CRC, Fig. 3(c) shows the normalized intensity value of $P(r_s)$ at $r_s = r_{s,\text{optimal}}$ for the four subject groups ordered in increasing aggressiveness from left to right. Consistent with Figs. 3(a) and 3(b), we see a progression toward a lower intensity as the polyp aggressiveness increases with a maximal 18% decrease between control and AA subject groups. This effect is statistically significant at the 5% level for nondiminutive adenomatous polyps (i.e., diameter ≥ 5 mm), an observation that is consistent with the earlier *ex vivo* CRC study.⁹

We note that the comparable curves for DA and A subjects omitted from Figs. 3(a) and 3(b) follow the same progression as

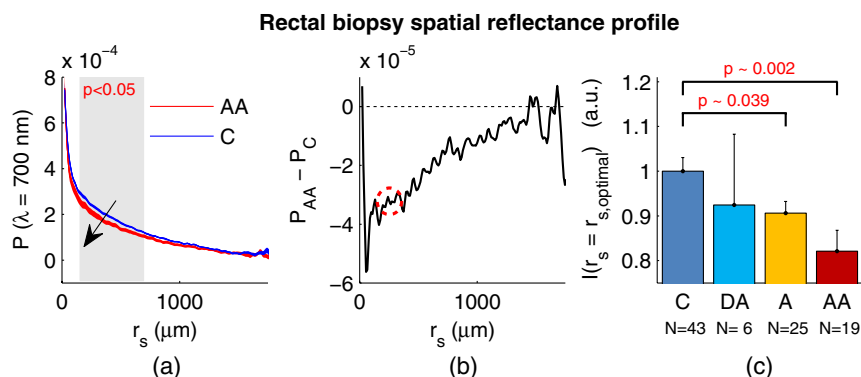


Fig. 3 CRC field carcinogenesis alterations measured in the shape of $P(r_s)$ from rectal biopsies. (a) Comparison between $P(r_s)$ for advanced adenomas (AA, diameter > 10 mm or adenocarcinoma) versus control (C) with the thickness of the curve indicating the standard error between measurements. The arrow indicates the direction of the change from AA to C and the gray shaded region indicates the values of r_s for which the curves are significantly different. (b) Difference (AA – C) between the curves shown in panel (a). The dotted circle indicates $r_{s,\text{optimal}}$ (i.e., the location of the most significant effect) of the difference curve. (c) Normalized intensity at $r_{s,\text{optimal}}$ for groups at increasing risk of CRC. DA, diminutive adenomas with diameter from 0 to 4 mm and A, adenomas with diameter from 5 to 9 mm.

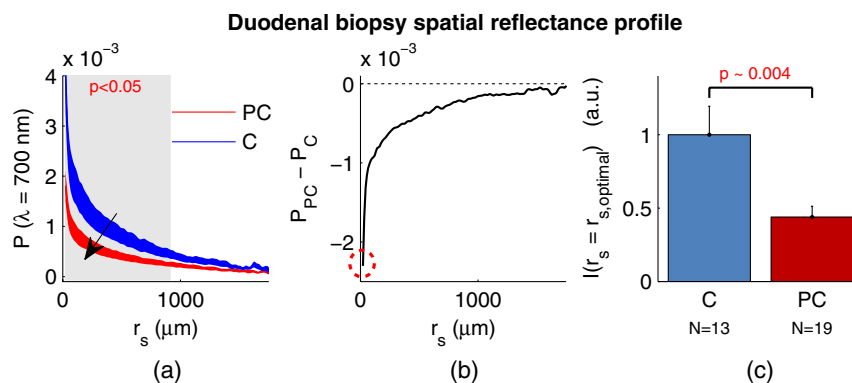


Fig. 4 Pancreatic cancer (PC) field carcinogenesis alterations measured in the shape of $P(r_s)$ from duodenal biopsies. (a) Comparison between $P(r_s)$ for PC versus control with the thickness of the curve indicating the standard error between measurements. The arrow indicates the direction of the change from PC to control and the gray shaded region indicates the values of r_s for which the curves are significantly different. (b) Difference (PC – C) between the curves shown in panel (a). The dotted circle indicates $r_{s,optimal}$ of the difference curve. (c) Normalized intensity at $r_{s,optimal}$ for PC and control groups.

demonstrated in Fig. 3(c). However, for figure clarity these data were not shown.

We repeated the above analysis for the PC study. Figure 4 shows the changes in $P(r_s)$ attributable to PC field carcinogenesis measured in *ex vivo* duodenal biopsies. Going from the curve for control subjects to those with PC, there is a downward and inward shift of $P(r_s)$, similar to the trend observed in CRC. We find a statistical significance over values of r_s ranging from ~20 to 900 μm . Figure 4(b) shows the difference between $P(r_s)$ for control and PC subjects. As r_s approaches 0, we find a monotonically increasing effect with $r_{s,optimal} = 20 \mu\text{m}$. Finally, Fig. 4(c) shows the normalized intensity value of

$P(r_s)$ at $r_s = r_{s,optimal}$ for control versus PC. This shows a 56% reduction in intensity from control to PC, which is statistically significant at the 5% level.

4.2 Ultrastructural Alterations in CRC and PC

In order to gain a more physical understanding of the structural composition that leads to the observed alterations in $P(r_s)$, we extracted the ultrastructural properties from the shape of $P(r_s)$ as described in Sec. 3. We note that this extraction routine assumes that the medium is composed of a single slab of random media, which follows the Whittle-Matérn model. As such, the

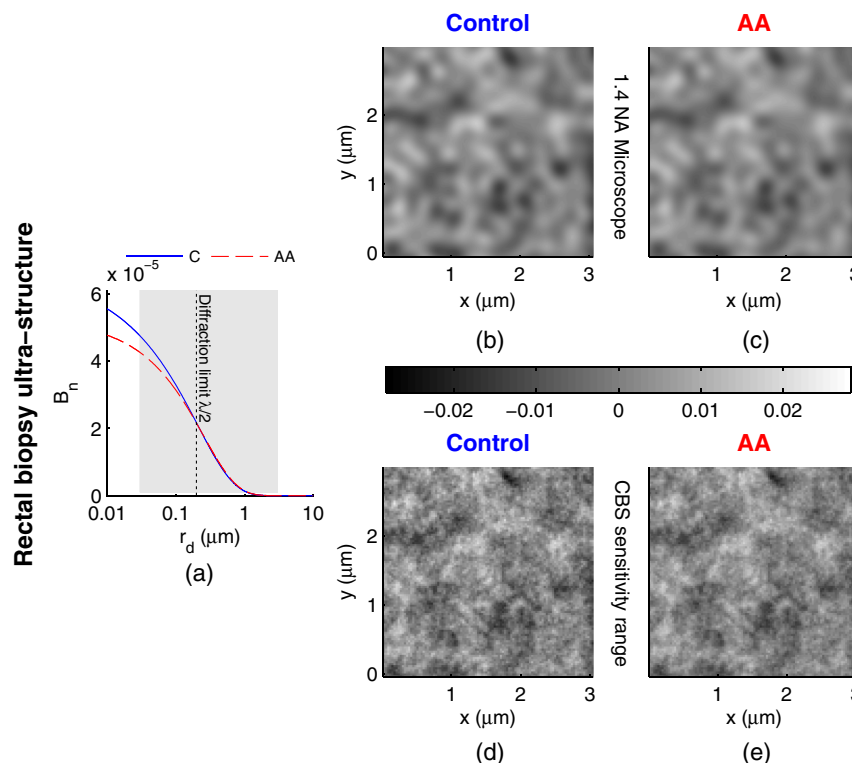


Fig. 5 Representations of the continuous random media extracted from the CRC study biopsy measurements. (a) $B_n(r_d)$ for control versus AA. The gray shaded region indicates the approximate range of values over which enhanced backscattering (EBS) is sensitive. (b) and (c) Continuous media realizations with 1.4 NA microscope resolution at $\lambda = 0.4 \mu\text{m}$ for the average ultrastructural properties of control and AA subjects, respectively. (d) and (e) Continuous media realizations over the EBS sensitivity range with the average ultrastructural properties of control and AA subjects, respectively.

extracted values provide estimates for the bulk ultrastructural and optical properties over the entire biopsy.

Figure 5(a) shows the shape of $B_n(r_d)$ corresponding to the mean ultrastructural properties extracted for the control and AA subjects in the CRC study. The gray shaded region indicates the approximate range of structural length-scales over which EBS is sensitive to the shape of $B_n(r_d)$ (~ 30 nm to 3 μm).¹³ Interestingly, a reduction in the value of $B_n(r_d)$ is seen within the subdiffractive regime ($r_d < \lambda/2$, $\lambda = 0.4$ μm), but is negligible for structural length-scales within the resolution limit of a conventional imaging system. This implies that the alterations observed in the shape of $P(r_s)$ are primarily attributable to minuscule structures that could not be resolved in a conventional light microscope. To better convey this idea, Figs. 5(b) and 5(c) depict 1.4 NA microscope resolution renderings of the random media described by the shapes of $B_n(r_d)$ for control and AA subjects, respectively. In these images, all subdiffractive structures have been blurred away, leaving larger fluctuations that are qualitatively indistinguishable between control and AA subjects.

In contrast with the microscope resolution images, Figs. 5(d) and 5(e) show renderings of the comparable random media with resolution (30 nm) and spatial extent (3 μm) chosen such that they match the structural length scale sensitivity of EBS. In this way, each rendering represents the range of structures that EBS “sees.” Comparison with the microscope resolution images demonstrates the sensitivity of EBS to much finer compositional details. Using this capability, it is possible to distinguish between control and AA subjects in Figs. 5(d) and 5(e), respectively. While the changes are very subtle, there is an appreciable

reduction in the presence of smaller structural length-scales for AA subjects.

Repeating this analysis for the PC study, Fig. 6(a) shows the shape of $B_n(r_d)$ that corresponds to the mean ultrastructural properties extracted for all control and PC subjects. Similar to the CRC study above, a reduction in the value of $B_n(r_d)$ is seen within the subdiffractive regime, but becomes negligible almost exactly at the diffraction limit. This higher-frequency detail is almost entirely blurred away in the microscope resolution images in Figs. 6(b) and 6(c). Depictions of the range of structures detected by EBS for control and PC subjects are shown in Figs. 6(d) and 6(e), respectively. In this case, two prominent alterations are visible: (1) a reduction in refractive index variance and (2) a reduction in the presence of smaller structural length-scales.

4.3 Optical Property Alterations in CRC and PC

To provide quantification of the measured field carcinogenesis changes in a way that is more comparable to other optical techniques, we convert the ultrastructural properties into optical properties using the analytical equations presented in Ref. 22. The values of l_s^* measured at $\lambda = 700$ nm, g measured at $\lambda = 700$ nm, and D for CRC biopsies are shown in Fig. 7. We note that D is included as an optical property in this plot since it demonstrates the spectral dependence of light transport (as described in Sec. 2). For all three optical properties, there is a statistically significant increase in value between C and AA subjects, with l_s^* increasing 12.6%, g increasing 1.9%, and D increasing 5.1%.

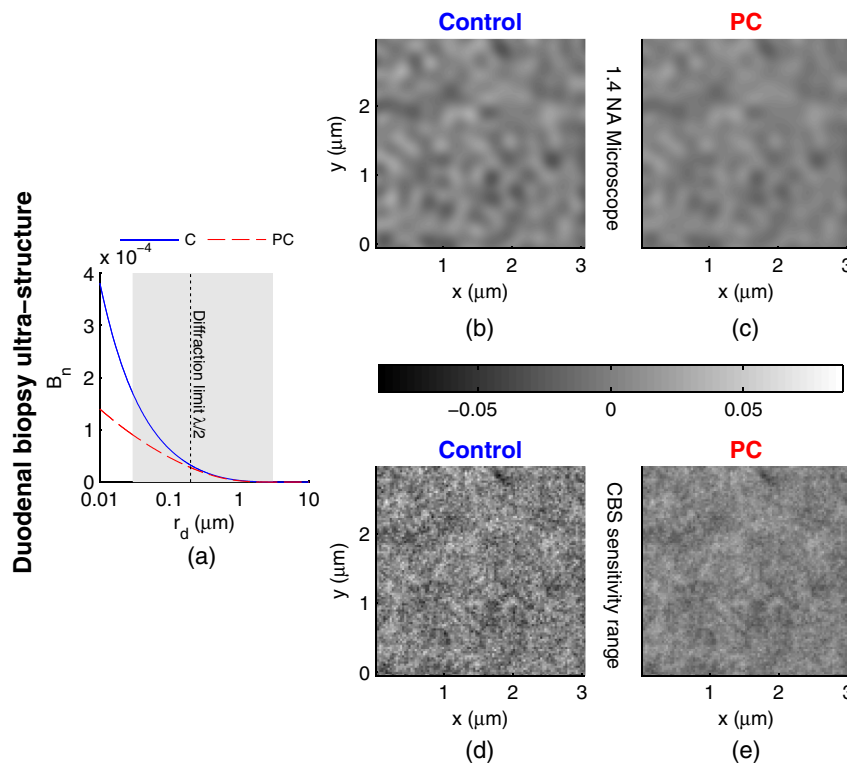


Fig. 6 Representations of the continuous random media extracted from the PC study biopsy measurements. (a) $B_n(r_d)$ for control versus PC. The gray shaded region indicates the approximate range of values over which EBS is sensitive. (b) and (c) Continuous media realizations with 1.4 NA microscope resolution at $\lambda = 0.4$ μm for the average ultrastructural properties of control and PC subjects, respectively. (d) and (e) Continuous media realizations over the EBS sensitivity range with the average ultrastructural properties of control and PC subjects, respectively.

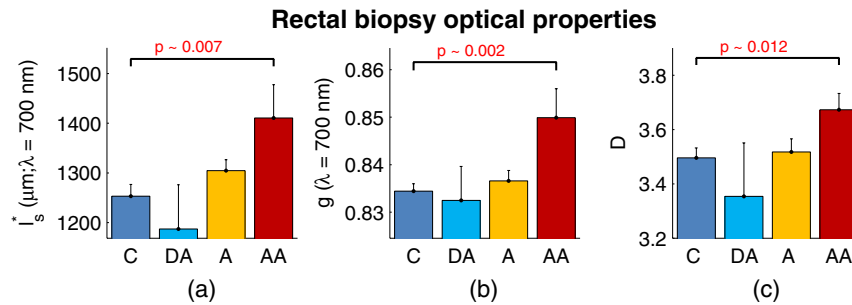


Fig. 7 Optical properties of rectal biopsies in the CRC study. (a) I_s^* measured at $\lambda = 700 \text{ nm}$. (b) g measured at $\lambda = 700 \text{ nm}$. (c) Each plot shows mean + standard error. $N = 43$ for C, $N = 6$ for DA, $N = 25$ for A, and $N = 19$ for AA.

Following the progression from C to A to AA, there is a smooth increase in value for each optical property. While the DA values in our dataset do not follow this trend, the large standard error on their measurement (due to relatively small sample size) does not preclude the possibility of a smooth progression with larger sample size. Indeed, based on the trend in Fig. 4(c) and the compounding multistep nature of carcinogenesis, this is likely the case.

The optical properties for biopsies in the PC study are shown in Fig. 8. Once again, for all three optical properties, there is a statistically significant increase in value, with I_s^* increasing 21.1%, g increasing 4.6%, and D increasing 66.9%. Interestingly, the directionality of the optical property changes in field carcinogenesis is the same for both CRC and PC.

4.4 Estimate of the Penetration Depth of Changes in CRC and PC

To obtain a better understanding of the depths at which the observed changes in $P(r_s)$ originate, we performed Monte Carlo simulations in which both r_s and the maximum depth z_{max} of each photon were tracked to generate 2-D $P(r_s, z_{\text{max}})$ distributions [shown in Figs. 9(a) and 10(a)]. Four simulations with optical properties corresponding to the mean values calculated for AA, CRC control, PC, and PC control were performed. For each simulation, a 2-D grid of $P(r_s, z_{\text{max}})$ with fixed spatial coordinates corresponding to the experimentally measured range of values was initiated. Light intensity was then deposited into the fixed $P(r_s, z_{\text{max}})$ grid positions until 10^{10} photon histories were computed.

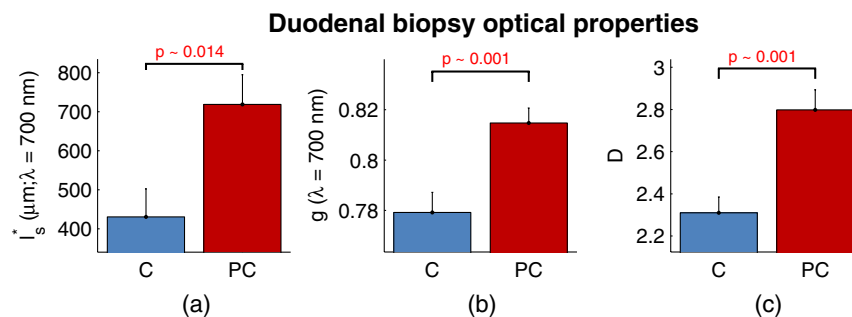


Fig. 8 Optical properties of duodenal biopsies in the PC study. (a) I_s^* measured at $\lambda = 700 \text{ nm}$. (b) g measured at $\lambda = 700 \text{ nm}$. (c) Each plot shows mean + standard error. $N = 13$ for C and $N = 19$ for PC.

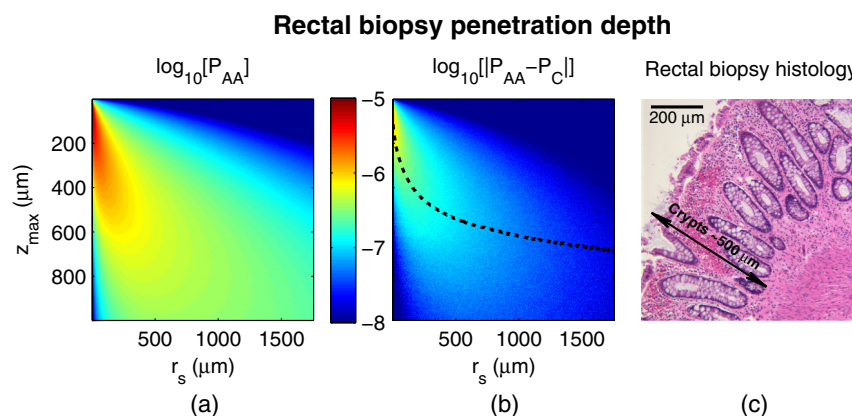


Fig. 9 Penetration depth of in CRC field carcinogenesis using Monte Carlo simulation. (a) Log-scale $P(r_s, z_{\text{max}})$ distribution for the average optical properties of all AA subjects. (b) Log-scale of the absolute difference in $P(r_s, z_{\text{max}})$ between control and AA subjects. The dashed black line indicates $\bar{z}_{\text{max}}(r_s)$. (c) Histological image from a rectal biopsy.

Figure 9 demonstrates the penetration depth of the $P(r_s)$ signal in CRC field carcinogenesis. The log-scale $P_{AA}(r_s, z_{\max})$ distribution corresponding to the average optical properties of all AA subjects is shown in Fig. 9(a) (P_C not shown since it is qualitatively very similar). As expected from multiply scattered light transport, with increasing values of r_s , there is a corresponding increase in z_{\max} . In order to isolate the location of the subtle differences in light propagation between control and AA subjects, Fig. 9(b) shows the absolute difference between $P_C(r_s, z_{\max})$ and $P_{AA}(r_s, z_{\max})$ in log-scale. Qualitatively, the location of the changes with the largest magnitude is found at very small values of r_s and z_{\max} . To better quantify the depth of these changes, we calculate the average penetration depth of the difference signal for each value of r_s as

$$\overline{z_{\max}}(r_s) = \frac{\int_0^{1000 \mu\text{m}} z_{\max} \cdot [P_{AA}(r_s, z_{\max}) - P_C(r_s, z_{\max})] dz_{\max}}{\int_0^{1000 \mu\text{m}} [P_{AA}(r_s, z_{\max}) - P_C(r_s, z_{\max})] dz_{\max}}. \quad (12)$$

The values of $\overline{z_{\max}}(r_s)$ are represented as the dashed black line in Fig. 9(b).

Conceptually, $\overline{z_{\max}}$ represents the approximate depth at which the alterations occur (given the understanding that a wide range of depths do, in fact, contribute). Comparing with the values of r_s for which the experimentally measured CRC $P(r_s)$ data are significantly separated [data shown in Fig. 3(a)], the depths at which the changes originate are between ~ 400 and $575 \mu\text{m}$ with the optimal difference occurring at $465 \mu\text{m}$ in depth. To qualitatively visualize the morphological structures interrogated over these depths, Fig. 9(c) shows a representative histological section acquired from one rectal biopsy. This image illustrates that the measured signal primarily originates from within the colonic crypts ($\sim 500 \mu\text{m}$ in length) and surrounding extracellular matrix, which composes the superficial mucosal layer.

Figure 10 repeats the penetration depth analysis of the $P(r_s)$ signal for PC field carcinogenesis. The log-scale $P_{PC}(r_s, z_{\max})$ distribution corresponding to the average optical properties of all PC subjects is shown in Fig. 10(a). Figure 10(b) shows the absolute difference between P_C and P_{AA} in log-scale with the values of $\overline{z_{\max}}(r_s)$ represented as the dashed black line. Comparing with the values of r_s for which the experimentally measured PC data are significantly separated [data shown

in Fig. 4(a)], the depths at which the signal originates are between ~ 100 and $500 \mu\text{m}$ with the optimal difference occurring at $100 \mu\text{m}$ in depth. The representative histological section from one duodenal biopsy shown in Fig. 10(c) indicates that these depths correspond to the superficial mucosal layer, which is composed of villi, crypts, and the surrounding extracellular matrix.

5 Discussion and Conclusions

In many ways, EBS is the ideal technique to use when studying bulk light transport in biological tissue.

From a utilization perspective, it offers an easy-to-implement instrument that enables noncontact measurements of intrinsic scattering and absorption contrast (no staining needed). In addition, due to the collimated beam delivery of light to the sample, EBS possesses a large tolerance in sample positioning (over 20 cm range in sample positioning has no effect on the signal). This allows measurement of nonstationary targets to be acquired without inducing error or motion artifacts. Moreover, since measurements are taken in reflection as opposed to transmission, tissue can be quantified *in situ* without sectioning or other preparation.

From a theoretical perspective, the high spatial resolution measurement of $P(r_s)$ at subdiffusion length-scales is extremely sensitive to the shape of the differential scattering function per unit volume $\sigma(\theta)$.^{7,11,12} This allows extraction of not only parameters such as l_s , g , and D , which define the shape of $\sigma(\theta)$, but also in principle the full shape of $\sigma(\theta)$. Furthermore, the shape of $\sigma(\theta)$ is directly related to the shape of $B_n(r_d)$ through Fourier transformation, enabling quantification of ultrastructural components down to $\sim 30 \text{ nm}$ in size (i.e., approximately one order of magnitude smaller than the diffraction limit).¹³ Finally, because the signal within the subdiffusion regime is primarily generated by the superficial depths of a scattering medium, an added benefit of EBS is its sensitivity to the superficial mucosal layers where epithelial cancers originate. Within the mucosal layer, specific depths can then be targeted by analyzing the signal at different values of r_s .³⁷

In this paper, we utilized these benefits of EBS to determine the values of r_s for which $P(r_s)$ is significantly altered in field carcinogenesis, extracted the structural composition and optical properties that lead to such changes, and estimated the depth at which the changes occur. Interestingly, in both the CRC and PC

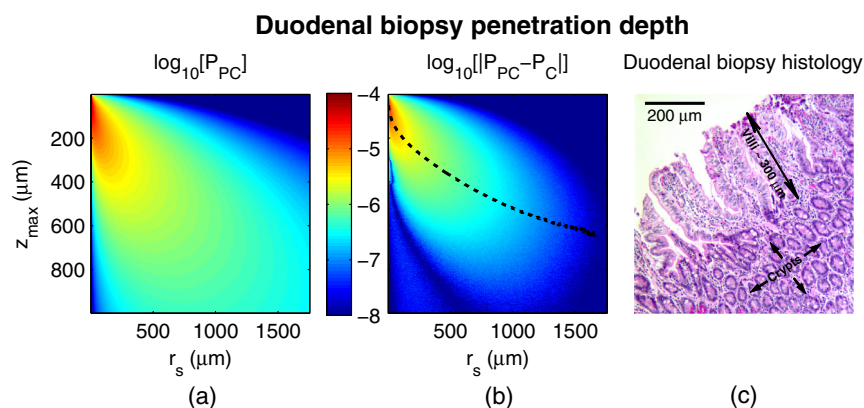


Fig. 10 Penetration depth of $P(r_s)$ in PC field carcinogenesis using Monte Carlo simulation. (a) Log-scale $P(r_s, z_{\max})$ distribution for the average optical properties of all PC subjects. (b) Log-scale of the absolute difference in $P(r_s, z_{\max})$ between control and PC subjects. The dashed black line indicates $\overline{z_{\max}}(r_s)$. (c) Histological image from a duodenal biopsy.

studies, we found a similar directionality of the changes in $P(r_s)$, $B_n(r_d)$, and optical properties.

1. For $P(r_s)$, with progression toward a more diseased state, we found a statistically significant downward and inward shift in shape occurring at length-scales smaller than ~ 1 mm. The magnitude of the effect (quantified as the difference between disease and control) was reduced with increasing values of r_s , suggesting that structural alterations in the superficial mucosal layer are responsible for a majority of the observed signal.

In CRC, we found a significant decrease in $P(r_s)$ for $r_s = 150$ to $700 \mu\text{m}$, with the most significant change occurring at $r_s = 267 \mu\text{m}$. This corresponds to average penetration depths between ~ 400 and $575 \mu\text{m}$, with the optimal difference occurring at $465 \mu\text{m}$ in depth. Morphologically, this signal is attributed to structures within the colonic crypts and surrounding extracellular matrix.

In PC, we found a significant decrease in $P(r_s)$ for $r_s = 20$ to $900 \mu\text{m}$, with the most significant change occurring at $r_s = 20 \mu\text{m}$. This corresponds to average penetration depths between ~ 100 and $500 \mu\text{m}$, with the optimal difference occurring at $100 \mu\text{m}$ in depth. Morphologically, this signal is attributed to structures within the duodenal villi, crypts, and surrounding extracellular matrix.

2. For $B_n(r_d)$, there was an appreciable decrease in structural correlation only for values of r_d smaller than the diffraction limit of violet light ($\lambda/2 = 200$ nm). Thus, the physical alterations in field carcinogenesis measured by EBS occur at structural length-scales smaller than the resolution of a conventional light microscope and, therefore, would be difficult or impossible to detect with such instruments. Physically, this change in $B_n(r_d)$ is attributable to a reduction in the quantity of structures with size between 30 and 200 nm.
3. For each of the three optical properties (l_s^* , g , and D), we found an increase in value for the diseased tissue. In the CRC study, we found l_s^* increases 12.6%, g increases 1.9%, and D increases 5.1%. In the PC study, we found an even larger effect with l_s^* increasing 21.1%, g increasing 4.6%, and D increasing 66.9%.

Furthermore, the changes observed in the current study are in agreement with the decrease in LEBS enhancement factor E and spectral slope SS observed in the previous *ex vivo* bench-top LEBS PC and CRC studies^{9,10} and current *in vivo* optical probe LEBS PC and CRC studies.^{4,15-17} This can be confirmed by looking at the definitions of E and SS : The empirical parameter E can be found as $E = \int_0^\infty P(r_s) \cdot C(r_s) dr_s$, where $C(r_s)$ is the spatial coherence function [a decaying function that focuses on $P(r_s)$ at short length scales]. As such, the decrease in $P(r_s)$ at short length scales observed in the current study is consistent with a decrease in E . Moreover, this decrease in E is consistent with the increase in l_s^* in the current study since $E \propto 1/l_s^*$ (Ref. 31). The empirical parameter SS is the negative slope of a linear regression line fit to $E(\lambda)$ and can be related to D

as $D = -SS \cdot \langle \lambda \rangle \langle E \rangle^{-1} + 3$, where $\langle \cdot \rangle$ indicates the average over the entire wavelength range.³¹ Thus, the increase in D for the current study is consistent with a decrease in SS . The consistency between all studies provides corroboration for the changes presented in the current study.

The fact that the observed changes occurred with similar directionality for both the CRC and PC studies suggests the existence of a common progression of structural transformations in the early stages of these two types of cancer (and potentially for a majority or even all cancers). In other words, although both cancers emerge through a unique sequence of genetic alterations, the resulting structural phenotype manifests itself in a similar way as both diseases progress. This is understandable as the fundamental objective of all cancers is to create an environment that promotes cell survival, proliferation, and eventual metastasis.

While the statistical nature of these ultrastructural alterations was quantified in the current study, the specific structures that contribute to the observed effect cannot be determined directly using EBS. Nonetheless, we can conclude that the signal is localized to superficial depths within the mucosa. The implication for clinical diagnosis is that short penetration depths need to be targeted in order to achieve optimal performance. Mechanistically, this provides a general road map of which morphological structures to investigate. Ongoing research to implicate specific mucosal components suggests that the alterations occur due to a combination of intracellular (e.g., condensation of chromatin in the nucleus²⁻⁴ or abnormalities in the cytoskeleton⁵) and extracellular components (e.g., collagen cross-linking^{4,6}). Interestingly, these changes appear to be attenuated versions of other classical markers of neoplasia.⁴ Chromatin compaction at larger length-scales ($>0.5 \mu\text{m}$) is a hallmark of dysplasia widely used in histopathology,³⁹ and lysyl oxidase (LOX)-induced collagen cross-linking is a well-known hallmark of tumor microenvironment.^{40,41} Thus, the changes detected in field carcinogenesis are largely the same as those occurring at the site of a focal tumor, only muted in magnitude. A forthcoming paper will provide 3-D spatial maps of the ultrastructural/optical alterations occurring within CRC and PC mucosa using inverse spectroscopic optical coherence tomography.⁴²⁻⁴⁴

Acknowledgments

This study was supported by National Institutes of Health grant numbers RO1CA128641 and R01EB003682. A. J. Radosevich is supported by a National Science Foundation Graduate Research Fellowship under Grant No. DGE-0824162.

References

1. D. P. Slaughter, H. W. Southwick, and W. Smejkal, "Field cancerization in oral stratified squamous epithelium. Clinical implications of multicentric origin," *Cancer* **6**(5), 963-968 (1953).
2. Y. Stypula-Cyrus et al., "Hdac up-regulation in early colon field carcinogenesis is involved in cell tumorigenicity through regulation of chromatin structure," *PLoS ONE* **8**(5), e64600 (2013).
3. J. S. Kim et al., "The influence of chromosome density variations on the increase in nuclear disorder strength in carcinogenesis," *Physical Biology* **8**(1), 015004 (2011).
4. V. Backman and H. K. Roy, "Advances in biophotonics detection of field carcinogenesis for colon cancer risk stratification," *J. Cancer* **4**(3), 251-261 (2013).
5. N. N. Mutyal et al., "Biological mechanisms underlying structural changes induced by colorectal field carcinogenesis measured with

- low-coherence enhanced backscattering (LEBS) spectroscopy," *PLoS One* **8**(2), e57206 (2013).
6. V. Backman and H. K. Roy, "Light-scattering technologies for field carcinogenesis detection: a modality for endoscopic prescreening," *Gastroenterology* **140**(1), 35–41 (2011).
 7. A. J. Radosevich et al., "Polarized enhanced backscattering spectroscopy for characterization of biological tissues at subdiffusion length scales," *IEEE J. Sel. Topics Quantum Electron.* **18**(4), 1313–1325 (2012).
 8. Y. L. Kim et al., "Depth-resolved low-coherence enhanced backscattering," *Opt. Lett.* **30**(7), 741–743 (2005).
 9. H. K. Roy et al., "Association between rectal optical signatures and colonic neoplasia: potential applications for screening," *Cancer Res.* **69**(10), 4476–4483 (2009).
 10. V. Turzhitsky et al., "Investigating population risk factors of pancreatic cancer by evaluation of optical markers in the duodenal mucosa," *Dis. Markers* **25**(6), 313–321 (2008).
 11. A. J. Radosevich et al., "Measurement of the spatial backscattering impulse-response at short length scales with polarized enhanced backscattering," *Opt. Lett.* **36**(24), 4737–4739 (2011).
 12. E. Vitkin et al., "Photon diffusion near the point-of-entry in anisotropically scattering turbid media," *Nat. Commun.* **2**, 587 (2011).
 13. A. J. Radosevich et al., "Structural length-scale sensitivities of reflectance measurements in continuous random media under the born approximation," *Opt. Lett.* **37**(24), 5220–5222 (2012).
 14. N. N. Mutyal et al., "A fiber optic probe design to measure depth-limited optical properties in-vivo with low-coherence enhanced backscattering (LEBS) spectroscopy," *Opt. Express* **20**(18), 19643–19657 (2012).
 15. N. N. Mutyal et al., "In-vivo risk stratification of pancreatic cancer by evaluating optical properties in duodenal mucosa," in *Biomedical Optics and 3-D Imaging*, p. BSu5A.10, Optical Society of America, Washington, DC (2012).
 16. N. N. Mutyal et al., "In vivo pancreatic cancer risk analysis by duodenal interrogation with low coherence enhanced backscattering spectroscopy," *Clin. Can. Res.* (in preparation).
 17. N. N. Mutyal et al., "In-vivo risk stratification of colon carcinogenesis by measurement of optical properties with novel lens-free fiber optic probe using low-coherence enhanced backscattering spectroscopy (LEBS)," in *Conference 8230: Biomedical Applications of Light Scattering VI* (2012).
 18. M. Born and E. Wolf, *Principles of Optics: Electromagnetic Theory of Propagation, Interference and Diffraction of Light*, 7th ed., Cambridge University Press, Cambridge, UK (1999).
 19. H. van de Hulst, *Light Scattering by Small Particles*, Dover, New York (1981).
 20. C. F. Bohren and D. R. Huffman, *Absorption and Scattering of Light by Small Particles*, John Wiley and Sons, New York (1983).
 21. A. Ishimaru, *Wave Propagation and Scattering in Random Media. Volume I: Single Scattering and Transport Theory*, Academic Press, New York (1978).
 22. J. D. Rogers, İ. R. Çapoğlu, and V. Backman, "Nonscalar elastic light scattering from continuous random media in the born approximation," *Opt. Lett.* **34**(12), 1891–1893 (2009).
 23. C. J. R. Sheppard, "Fractal model of light scattering in biological tissue and cells," *Opt. Lett.* **32**(2), 142–144 (2007).
 24. J. M. Schmitt and G. Kumar, "Turbulent nature of refractive-index variations in biological tissue," *Opt. Lett.* **21**(16), 1310–1312 (1996).
 25. P. Guttorp and T. Gneiting, "Studies in the history of probability and statistics xlix on the matérn correlation family," *Biometrika* **93**(4), 989–995 (2006).
 26. Y. Kuga and A. Ishimaru, "Retroreflectance from a dense distribution of spherical particles," *J. Opt. Soc. Am. A* **1**(8), 831–835 (1984).
 27. L. Tsang and A. Ishimaru, "Backscattering enhancement of random discrete scatterers," *J. Opt. Soc. Am. A* **1**(8), 836–839 (1984).
 28. P. E. Wolf and G. Maret, "Weak localization and coherent backscattering of photons in disordered media," *Phys. Rev. Lett.* **55**(24), 2696–2699 (1985).
 29. M. P. V. Albada and A. Lagendijk, "Observation of weak localization of light in a random medium," *Phys. Rev. Lett.* **55**(24), 2692–2695 (1985).
 30. A. J. Radosevich et al., "Open source software for electric field Monte Carlo simulation of coherent backscattering in biological media containing birefringence," *J. Biomed. Opt.* **17**(11), 115001 (2012).
 31. V. Turzhitsky et al., "Measurement of optical scattering properties with low-coherence enhanced backscattering spectroscopy," *J. Biomed. Opt.* **16**(6), 067007 (2011).
 32. T. J. Farrell, M. S. Patterson, and B. Wilson, "A diffusion theory model of spatially resolved, steady-state diffuse reflectance for the noninvasive determination of tissue optical properties in vivo," *Med. Phys.* **19**(4), 879–888 (1992).
 33. A. Kienle et al., "Spatially resolved absolute diffuse reflectance measurements for noninvasive determination of the optical scattering and absorption coefficients of biological tissue," *Appl. Opt.* **35**(13), 2304–2314 (1996).
 34. R. Reif, O. A' Amar, and I. J. Bigio, "Analytical model of light reflectance for extraction of the optical properties in small volumes of turbid media," *Appl. Opt.* **46**(29), 7317–7328 (2007).
 35. A. Amelink and H. J. C. M. Sterenborg, "Measurement of the local optical properties of turbid media by differential path-length spectroscopy," *Appl. Opt.* **43**(15), 3048–3054 (2004).
 36. G. Zonios et al., "Diffuse reflectance spectroscopy of human adenomatous colon polyps in vivo," *Appl. Opt.* **38**(31), 6628–6637 (1999).
 37. A. J. Radosevich et al., "Depth-resolved measurement of mucosal microvascular blood content using low-coherence enhanced backscattering spectroscopy," *Biomed. Opt. Express* **1**(4), 1196–1208 (2010).
 38. A. J. Radosevich and J. D. Rogers, "Biophotonics Laboratory at Northwestern University," <http://biophotonics.bme.northwestern.edu/resources/index.html> (25 August 2013).
 39. D. Zink, A. H. Fischer, and J. A. Nickerson, "Nuclear structure in cancer cells," *Nat. Rev. Cancer* **4**(9), 677–687 (2004).
 40. H. E. Barker, T. R. Cox, and J. T. Erler, "The rationale for targeting the LOX family in cancer," *Nat. Rev. Cancer* **12**(8), 540–552 (2012).
 41. A.-M. Baker et al., "The role of lysyl oxidase in src-dependent proliferation and metastasis of colorectal cancer," *J. Natl. Cancer Inst.* **103**(5), 407–424 (2011).
 42. J. Yi et al., "Spatially-resolved optical and ultrastructural properties in the field effect of pancreatic and colorectal cancer observed by inverse spectroscopic optical coherence tomography," *J. Biomed. Opt.* (under review).
 43. J. Yi et al., "Can OCT be sensitive to nanoscale structural alterations in biological tissue?," *Opt. Express* **21**(7), 9043–9059 (2013).
 44. J. Yi and V. Backman, "Imaging a full set of optical scattering properties of biological tissue by inverse spectroscopic optical coherence tomography," *Opt. Lett.* **37**(21), 4443–4445 (2012).